ADVANCED MATERIALS TECHNOLOGIES
www.advmattechnol.de

Fabrication and Characterization of a Magnetic 3D-printed Microactuator

Florian Rothermel, Simon Thiele, Chris Jung, Anna Krapf, Sven Erik Ilse, Benoit Merle, Harald Giessen, and Alois M. Herkommer**

Conventional MEMS microactuators have, in recent years, been complemented by 3D-printed actuatable microstructures fabricated via two-Photon-Polymerization (2PP). Herein, a novel compact 3D-printed magnetically actuatable microactuator with a diameter of 500µm is demonstrated, originally designed for micro-optical systems. It is fabricated by incorporating a composite of NdFeB microparticles and epoxy resin into a designated reservoir of the printed mechanical structure within a simple post-processing step. The microactuator structure features mechanical springs, allowing for continuous positioning with large displacement. Mechanical studies by nanoindentation of IP-S bulk structures reveal a viscoelastic material behavior, described by a two-element General Kelvin-Voigt viscoelasticity model. The obtained material parameters are then used to simulate and characterize the spring behavior of the microactuator. Actuation experiments are conducted using an external microcoil. The actuator displacement is measured for triangular current pulses with a peak current of 106 mA and durations of 1 to 100 s, resulting in displacements of 69.1 to 88.9 µm. Hysteretic behavior of the actuator is observed, attributable to viscoelasticity and magnetic properties of the core material. Numerical simulations of the experiment demonstrate this behavior as well. On-the-fly demagnetization and the implementation of closed-loop control allow for both high repeatability and precise positioning.

1. Introduction

Actuation at the microscale is often accomplished by conventional microelectromechanical system (MEMS) actuators. Using well-established semiconductor fabrication methods, they can be easily manufactured not only as prototypes, but also in mass production. Typical actuation methods rely on electrostatic, piezoelectric, electrothermal, shape-memory, pneumatic, hydraulic, or electromagnetic effects.[1,2] Electrostatic actuators require high voltages and achieve only small forces and displacements. Larger forces are possible with piezoelectric actuation, which, however, is limited in displacement as well. In contrast, electrothermal, shape-memory alloy, pneumatic, and hydraulic actuators provide both, large forces and large displacements, but they generally suffer from lower response times. Therefore, electromagnetic actuation is particularly interesting, as it allows for high forces and large displacement, while it also enables fast responses.[3]

F. Rothermel, A. M. Herkommer
Institute of Applied Optics
University of Stuttgart
Pfaffenwaldring 9, 70569 Stuttgart, Germany
E-mail: rothermel@ito.uni-stuttgart.de; herkommer@ito.uni-stuttgart.de

S. Thiele
Printoptix GmbH
Nobelstr. 15, 70569 Stuttgart, Germany

C. Jung
Mikrop AG
Industriestr. 22, Wittenbach 9300, Switzerland

A. Krapf
Department Materials Science and Engineering
Friedrich-Alexander-University Erlangen-Nuremberg
Martensstr. 5, 91058 Erlangen, Germany

S. E. Ilse
Max-Planck Institute for Solid State Research
Heisenbergstr. 1, 70569 Stuttgart, Germany

B. Merle
Institute of Materials Engineering
University of Kassel
Mönchebergstr. 3, 34125 Kassel, Germany

H. Giessen
4th Physics Institute
University of Stuttgart
Pfaffenwaldring 57, 70569 Stuttgart, Germany

The ORCID identification number(s) for the author(s) of this article can be found under https://doi.org/10.1002/admt.202302196

DOI: 10.1002/admt.202302196

In recent years, classical fabrication of microactuators has been complemented by additive manufacturing.[4] Stereolithography (SLA) was used to fabricate a planar electrothermally actuatable microgripper, as well as an electromagnetic actuator.[5,6] Furthermore, fused deposition modeling (FDM) enables direct 3D printing of magnets and magnetically actuatable structures, using magnetic composite materials.[7–10] The potential for further miniaturization of actuators to attain overall sizes in the sub-millimeter range is however limited by the resolution constraints of these methods. Therefore, two-photon polymerization (2PP) by direct laser writing is of special interest for the fabrication of actuatable 3D microstructures,[11,12] which find applications in biomedicine,[13–15] microgrippers,[16,17] microrobotics, and sensors.[18–24] The large advantage of this fabrication method is its versatility, not only in terms of design freedom, but also regarding choice of printable photoresists. The latter enables so-called 4D-printing, which means the ability to directly fabricate mechanical structures consisting of stimuli-responsive materials, e.g., hydrogels, poly(N-isopropylacrylamide)(pNIPAM), or liquid crystal elastomers (LCEs). This has led to the demonstration of various microactuators that can be controlled via external stimuli, such as temperature,[25–28] light,[29–32] pH-value, or combinations of them.[33–36] While these actuators are applicable for many different scenarios, they are also often restricted by, e.g., requiring aqueous environments, high temperatures or special setups for fabrication or for the actuation.

Other approaches focus on electrostatic or magnetic actuation.[14,37–46] Especially the latter has been demonstrated in various applications, since it offers several advantages, such as easy integration into the 2PP fabrication process, remote control by external magnetic fields, as well as biocompatibility. The fabrication of such actuators is mainly achieved by directly incorporating magnetic particles into the polymerizable precursor or by adding ferromagnetic materials in post-processing steps, e.g., by deposition.[40,41] In other fabrication variants, magnetic beads are added to the resin,[42,44,46,47] which can be oriented and aligned via external magnetic fields during the printing process and thus, be directly connected to the microstructure. Nonetheless, these methods interfere in some way with the conventional 2PP fabrication method, such that it sets limitations on its flexibility. Printing on special substrates, e.g., optical fibers, could prove problematic, if the setup has to be altered. Composite magnetic resins could limit further functionalization of the microstructure, e.g., for microoptical applications, since multimaterial-processes would be involved. This issue can be addressed by a post-process incorporation of magnetic materials. Metal layer deposition is a viable choice, but the design-freedom is limited, as it cannot be selectively applied to desired regions and therefore sacrificial protection structures need to be implemented.

In this work, we present a magnetic microactuator, which consists of a monolithic 3D-printable structure that can be functionalized in a post-processing step by filling liquid composites of two-component epoxy resins and Neodymium-Iron-Boron (NdFeB) microparticles in dedicated reservoirs. The composite is then magnetized after curing, leaving a permanent magnet embedded in the mechanical microstructure. By implementing a mechanical spring, the structure can then be actuated and axially displaced through external magnetic fields. This method and a similar actuator have already been demonstrated in previous work for the actuation of microoptical elements,[43] but aside from that, we believe that applications in other scientific fields are also possible, such as endoscopic micromanipulation. Many applications require accurate positioning of the actuator, which is often aggravated by system-inherent non-linearities. Therefore, the behavior of the implemented system has to be known. Herein, we characterize a magnetic 3D-printed microactuator by first examining mechanical properties of the polymerized IP-S resin through nanoindentation tests. As the polymer exhibits viscoelastic behavior, the material properties and resulting spring characteristics are described using the generalized Kelvin-Voigt (GKV) viscoelasticity model. To demonstrate the capabilities of the actuator, we conducted actuation experiments to characterize the displacement behavior of the actuator corresponding to time varying magnetic fields. It is shown that the actuator displacement has a non-linear and hysteretic behavior that is caused by the viscoelasticity, as well as magnetic hysteresis of the external magnetic field generation. We demonstrate how these shortcomings can be counteracted by incorporating on-demand demagnetization and closed-loop control.

2. Results and Discussion

2.1. Actuator Design and Fabrication Method

The design of the microactuator is essentially comprised of two components, which are merged in one monolithic 3D-printable structure (**Figure 1A**). Three helical springs are used as mechanically flexible component to hold a ring-shaped fillable reservoir. While one spring might be sufficient, it is better to have more contact points for the reservoir to ensure stability during the printing process. A rectangular cross-section was chosen for the spring wire, since we found that the resulting spring stiffness is better controllable through design. The stiffness is furthermore dependent on other geometrical aspects, such as the spring diameter and its number of turns, as well as the mechanical properties of the polymerized resin, which depends not only on the resin itself, but also on the writing parameters, i.e., the degree-of-conversion (DC) as has been shown by others.[48–52] An experimental investigation of the spring design was conducted to achieve deformations greater than 100 µm with the expected magnetic forces, but also an adequate spring stiffness to withstand environmental forces, such as gravitation. We found a spring wire cross-section of $18 \times 12.5\ \mu m^2$ to be suitable for this purpose. The reservoir of the actuator has the shape of a hollow cylinder with an outer diameter of 500 µm, an inner diameter of 200 µm, an open top side and a perforated outer wall. The perforation with rectangular holes of size $25 \times 30\ \mu m^2$ augments the wettability of the reservoir and reduces agglomeration of magnetic particles at the outer wall during the filling procedure. Furthermore, small rectangular blocks are circularly distributed around the center at the bottom of the reservoir, serving as additional capillary structure. The flat surface in the center of the reservoir was implemented as reference for the optical displacement measurements. The final design has an an overall height of 650 µm.

As it is shown in Figure 1B, the fabrication of the microactuator consists of four process steps. The mechanical structure is printed using dip-in laser lithography (DiLL) with the proprietary

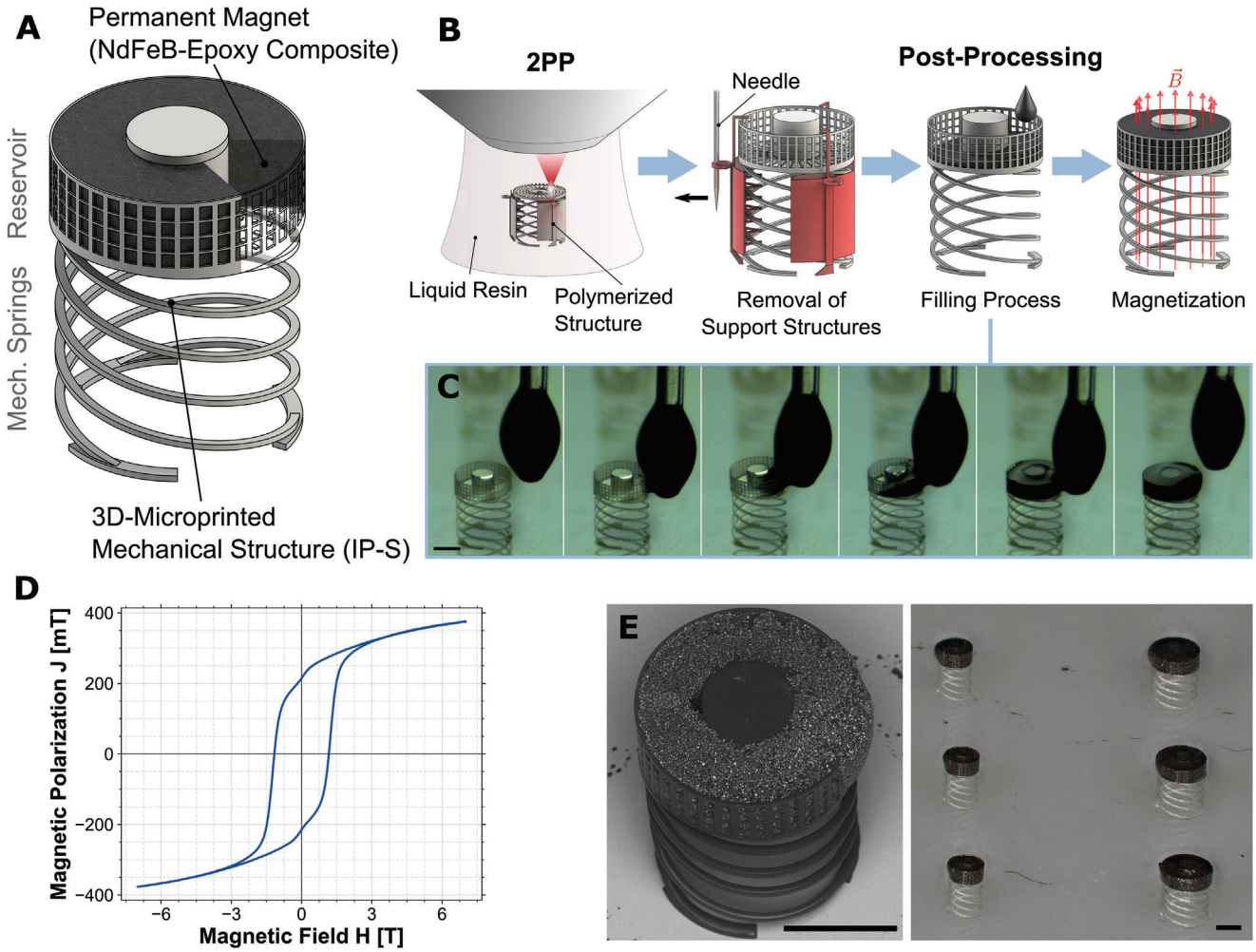

Figure 1. Microactuator design and fabrication process. A) Illustration of the 3D-printed microactuator, which consists of a mechanical spring attached to a permanent magnet. B) The fabrication process involves the 3D-printing of the mechanical structure via 2PP, as well as three post-processing steps. First, sacrificial support structures are removed and the reservoir of the microactuator filled afterward with a NdFeB-epoxy-composite. Finally, the composite is magnetized within a strong uniform magnetic field after curing. C) Images taken during the filling procedure. This is also provided as video in the Video S2 (Supporting Information). D) Magnetic hysteresis measurement of the composite within reservoir geometries of equal volume. E) Electron micrograph of a microactuator with filled reservoir. Digital microscope image of an array of microactuators of diameters 500 and 350 µm. Scale bars are 250 µm.

photoresist IP-S (Nanoscribe GmbH & Co. KG) onto a microscope cover glass substrate. Together with the actuator, three sacrificial support structures are fabricated that prevent damaging of the springs during the development procedure. This damaging is mainly caused by shear forces that occur when immersing the structures in the developer liquid, as well as so-called stiction of the delicate wires due to capillary forces when the liquid evaporates. Therefore, the support structures are designed to constrain motions of the entire structure in all directions and prevent stiction through a comb-structure that blocks the spring coils, thus keeping them apart. To reduce the overall footprint of the actuator and thus allow for printing on narrow area substrates, the supporting structures are mounted within the gaps between the spring feet. After development, the support structures are removed by inserting a fine needle into an embedded eyelet and applying a pulling force until the adhesion to the substrate breaks. This process is shown in the Video S1 (Supporting Information). It is to note that supercritical drying could also be used after development such that the sacrificial support structures are not necessary. This was not tested, however, and using this method can also set limitations on the usable substrates, whereas the proposed method can be used even when printing on special substrates, such as optical fiber tips.

In the next post-processing step, the reservoir is filled with a ferromagnetic composite, which consists of a two-component epoxy resin mixed with NdFeB-microparticles. The filling procedure is shown in the image series in Figure 1C and also as video in Video S2 (Supporting Information). A droplet of the composite is brought in contact with the outer wall of the reservoir, where capillary forces cause a flow into the reservoir. It is often required to break and restore contact of the droplet, because either the flow stops or the structure tends to move too far into the droplet leading to contamination of the central surface or abrupt overfilling. It is to note that the supporting structures have to be re-

moved beforehand as they can cause undesired contamination of the spring wires during contact with the composite droplet. Furthermore, it is important that the composite viscosity is low enough to ensure the capillarity, such that the mixing ratio between epoxy and microparticles has to be carefully chosen. In an experimental evaluation, different mixing ratios of NdFeB-microparticles with a typical grain size of 5µm and a low viscous epoxy resin were filled into 3D-printed reservoirs in order to find the highest particle concentration viable for the described procedure. We eventually chose a mixture containing 71.4 %wt. magnetic particles (weight-ratio 5:2), which is a compromise of the achievable magnetic remanence and the applicability. Composites containing higher amounts of microparticles would increase the remanence of the magnet and thus sensitivity of the actuator, but are significantly more viscous or even paste-like and therefore not applicable.

After the composite is cured, it is finally pulse-magnetized within a strong homogeneous magnetic field with a peak flux density of approx. 4 T, resulting in permanent magnetization. A hysteresis curve of magnets of similar volume and equal mixing ratio has been measured with a SQUID magnetometer and is shown in Figure 1D. It can be seen that a magnetic field of 4 T is sufficient to achieve magnetic remanences >200 mT. This remanence is comparable to reported values of permanent magnets fabricated via micro-patterned molds.[53] During the magnetization process it is important to ensure that the samples are oriented as intended, since oblique magnetization directions will lead to undesired tilting when actuated. Once magnetized, errors can hardly be corrected since the spring compliance allows the magnet to evade a demagnetization field.

Fabricated microactuators are shown in the images in Figure 1E. The left side shows a SEM-image of a single microactuator with filled (unmagnetized) reservoir, where excess composite is clearly visible at the right outer side, which originates from the contact between droplet and reservoir during the filling process. On the right side, a microscope image of an array of actuators is shown. The array consists of actuators of diameters 350 and 500 µm. While only the latter is discussed here, it shows that the microactuator is scaleable.

2.2. Mechanical Characterization

Mechanical microstructures fabricated by 2PP are typically designed with the assumption of elastic material behavior. However, this assumption may not hold true in all cases, particularly when precise positioning or structural stability under constant load is required. This is because polymerized photoresins, similar to numerous other polymeric materials, display viscoelastic behavior.[54,55] The structures thus show typical characteristics such as creep and relaxation when load is applied and subsequently removed.

Previous material studies of two-photon polymerized resins by uniaxial compression tests or nanoindentation mainly focused on elastic parameters, e.g., Young's modulus.[48,49,51,52,56,57] We therefore studied the viscoelastic properties of IP-S through nanoindentation tests on 3D-printed blocks of size 400 µm × 400 µm × 25 µm. An electron micrograph of one of those blocks is displayed in **Figure** 2A. They were fabricated using the same writing parameters as for the actuator (see Experimental Section). We chose two different laser powers (25 and 30 mW) to test whether the viscoelastic properties are sensitive to differences in the writing process. No significant change was observed (see Section S2, Supporting Information), which is why only the measurement and evaluation of the structures printed with 25 mW is discussed here.

The nanoindentation tests to obtain viscoelastic parameters were conducted in a similar manner as described by Lu et al.,[58] using a conospherical nanoindenter tip. The applied time-dependent load profile $P(t)$ consists of a ramp load segment with constant load rate, followed by a holding segment which can be expressed as:

$$P(t) = \dot{P}_0 \left[t - H(t - t_0) \cdot (t - t_0) \right] \tag{1}$$

with the constant load rate $\dot{P}_0$, the start time of the hold segment t_0 and the Heaviside-function $H(t)$. Details are given within the Experimental Section. The target indentation depth was chosen small enough to ensure operation within the linear viscoelastic regime. In Figure 2B, the mean value of seven indentation depth measurements is plotted versus time. Every block was only measured once, nonetheless resulting in a highly repeatable measurement with an overall standard deviation less than 12 nm. During the hold segment, viscoelastic creep of the material can be observed, leading to a depth change of approximately 17%.

To access the viscoelastic properties of the material, we fitted the generalized Kelvin-Voigt (GKV) model to the measurement data. Since a one-element GKV model, also known as standard linear solid model, was insufficient for the description of the data, we chose a two-element model as it is depicted in the inset of Figure 2B. More elements did not improve the fit quality by means of the coefficient of determination (R^2). Details about the mathematical expressions of the model are given in Section S1 (Supporting Information). The fitted model exhibits strong agreement with the measured data and yields the parameters for the elastic and viscous components. The resulting elastic components are described by elastic moduli E_i and viscous components by relaxation times τ_i, which were obtained by taking the mean of the parameters of the separately fitted measurements. The plotted fit curve corresponds to the behavior according to these mean parameters denoted in the inset.

For evaluating the behavior of the spring structure, the resulting material parameters were passed to a mechanical finite element simulation of the microactuator 3D-model. As illustrated in Figure 2C, a load function $F_{\text{load}}(t)$ was applied in axial direction of the spring, resulting in an axial displacement. The load function is of the same shape as $P(t)$, with an initial ramp loading with arbitrary target load of 25 µN and a duration of 10 s until the holding segment. In addition, we investigated on the influence of shape deviations of the spring wire cross section. An increase of 0.5 and 1 µm in width and height of the rectangular cross-section was assumed, which can be caused by the limited lateral and axial resolution given by the effective voxel. The resulting simulated displacements versus time for the designed wire cross-section, as well as the two deviations is plotted in Figure 2D. Due to the viscoelastic nature of the material, the spring also suffers from creep that leads to a displacement increase of approximately 26.5% in all three cases during the holding segment of 50 s duration. As it

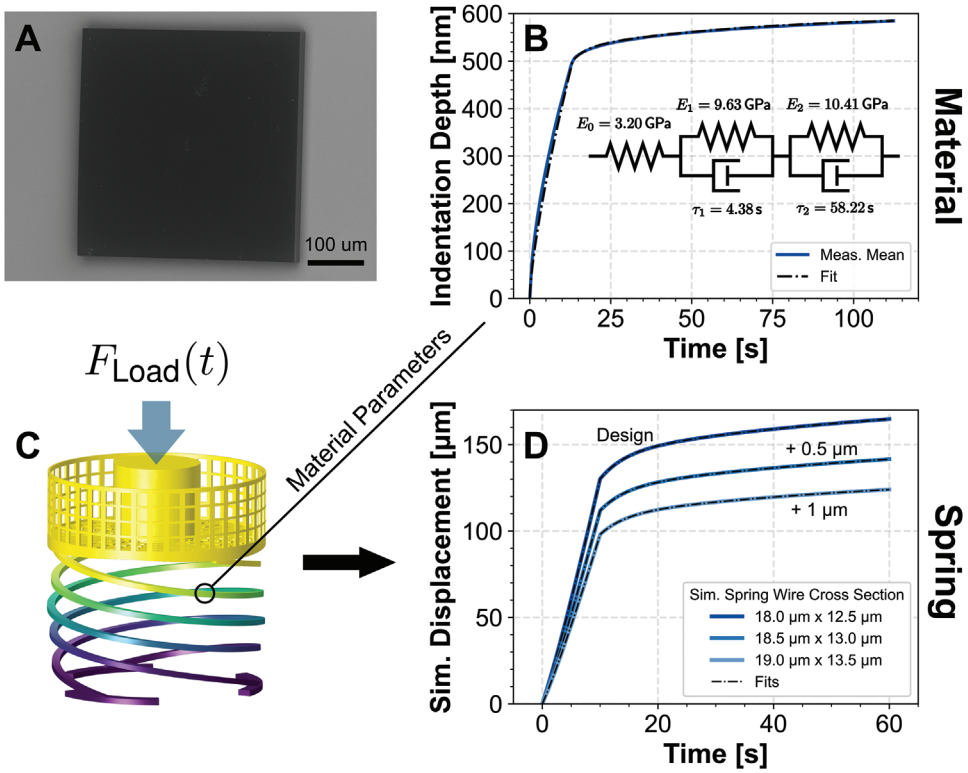

Figure 2. Mechanical characterization of the material and the spring of the microactuator. A) Electron micrograph of the polymerized IP-S blocks with a size of 400 × 400 × 25 µm^3 used for nanoindentation studies. B) Nanoindentation measurements showing the mean indentation depth versus time. Standard deviation is plotted as shaded region, but not visible due to highly repeatable measurements. The load profile consists of a ramp load to a target displacement of 500 nm followed by a hold segment of 100 s. During the hold segment, viscoelastic creep can be observed. Measurements were fitted separately using the generalized Kelvin-Voigt viscoelasticity model with two elements, which is depicted in the inset below the curves. The mean viscoelastic parameters E_i and τ_i of all fits were evaluated, which ultimately yield the plotted fit curve. C) Mechanical finite element simulation of the 3D model, using the viscoelastic parameters obtained from the nanoindenter measurements. The load function $F_{\text{Load}}(t)$ is again a ramp load followed by a hold segment. D) Simulated displacements versus time obtained from mechanical FEM simulations. These were conducted for the original spring design with a spring wire cross-sections of 18 × 12.5 µm^2, as well as slight increases of the width and height by 0.5 and 1 µm. The viscoelastic parameters describing the spring behavior are again obtained by fitting a two-element GKV model. The fit yields the parameters given in Table 1.

Table 1. Viscoelastic parameters obtained from fitting a two-element GKV model to the simulated spring behavior (shown in Figure 2D) with deviations of the spring wire cross-section.

Spring Wire Cross-Section	k_0 [N m^{-1}]	k_1 [N m^{-1}]	k_2 [N m^{-1}]	τ_1 [s]	τ_2 [s]
18 × 12.5 µm^2 (Design)	0.24	0.64	0.69	4.41	58.37
18.5 × 13 µm^2 (+ 0.5 µm)	0.28	0.74	0.80	4.42	60.00
19 × 13.5 µm^2 (+ 1 µm)	0.32	0.85	0.92	4.39	57.89

can be seen, the spring stiffness is significantly affected by deviations of the spring wire cross section.

The behavior of the spring can again be characterized with a two-element GKV-model. Therefore, the simulated displacement data was fitted for the three shown variants to obtain the elastic components, now described by the spring constants k_i, and the viscous components. The resulting parameters are displayed in **Table 1**. It is noticeable that the relaxation times of the spring for all variants are nearly the same as the ones of the material. Hence, it can be assumed that the structure itself does not affect the viscoelastic behavior.

2.3. Magnetic Actuation

Actuation experiments were conducted using the experimental setup illustrated in **Figure 3A**. A microcoil wound around an Iron-Nickel(FeNi) tube core functions as electromagnet to attract the magnetized composite inside the reservoir. We used a hollow instead of a bulk core in order to verify the applicability of the system in endoscopic implementations, utilizing 3D-printed micro-optics.[59] The attractive force between the electromagnet and the permanent magnet leads to a displacement of the actuator, which can be controlled by varying the coil current. Larger coil currents lead to larger magnetic field densities and thus to larger exerted magnetic forces, depending on the permeability and saturation magnetization of the core material. Furthermore, the magnetic force also non-linearly increases due to the displacement of the actuator, since the distance between the permanent magnet and the source of the external magnetic field, i.e., the coil, decreases. This ultimately leads to a non-linear relationship between actuator displacement and coil current. The setup was also implemented and extensively studied by finite element simulations, involving the magnetic, as well as the mechanical viscoelastic aspects of the experiment. It is to note that

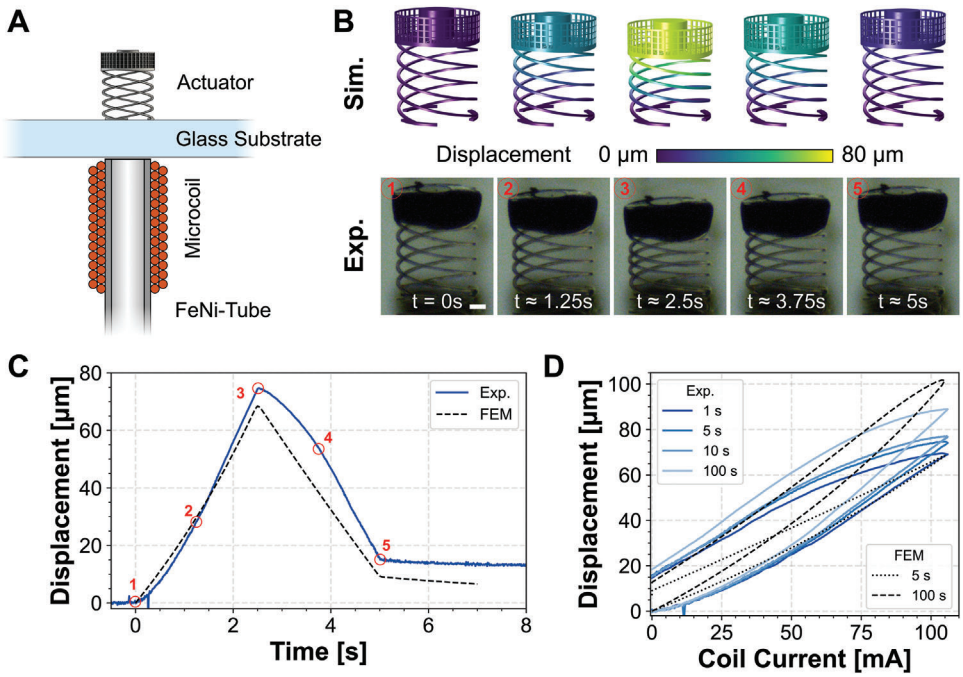

Figure 3. Actuation experiments. A) Illustration of the experimental setup. The microactuator is printed onto a glass substrate and displaced by the externally generated magnetic fields of a microcoil wound around an iron-nickel(FeNi)-tube core. B) Images and simulation of the microactuator during actuation with a triangular coil current profile with a rise and fall time of 2.5 s. The scale bar is 100 µm. A video of this experiment is provided in the Video S3 (Supporting Information). C) Plot of the displacement measurement versus time during the actuation, as well as numerically simulated data. The red circles highlight the displacement at the times specified in the images of the microactuator. D) Measured displacement plotted versus the applied coil current for durations of the triangular pulse of 1, 5, 10, and 100 s. A lowpass filter was applied to the displacement data of 10 and 100 s pulse duration to filter sudden spikes at small displacements. Finite element simulations for pulse durations of 1 and 100 s are plotted as well. The arrows denote the segments of a rising and falling current. The microactuator shows a non-linear and hysteretic behavior, depending on the coil current, as well as the pulse duration.

we assumed a deviation of the spring wire cross-section of 0.5 µm for the simulation, which shows a good resemblance of the experimental results.

During the experiments, the actuator samples were observed with a digital microscope. Figure 3B depicts images of a microactuator at the specified times during actuation with a symmetric triangular coil current profile of 2.5 s rise and fall times, with currents ranging from 0 to 106 mA. The starting time of the triangle pulse was denoted as $t = 0$ s. A video of the actuation is also provided in the Video S3 (Supporting Information). Images of a finite element simulation of the 3D-structure are also displayed within the same panel. The experimental results are in good agreement with the simulations. It is to note, however, that in contrast to the simulation, the microactuator shows slight tilting during the actuation experiment. This behavior was observed in all samples, while the extent differed from sample to sample. Therefore, it is likely that this results from distribution inhomogeneities of the NdFeB-microparticles inside the reservoir.

For the quantification of the microactuator displacement, a chromatic-confocal distance sensor was setup in axial direction in addition to the camera observation (see Figure S4, Supporting Information). The measurement corresponding to the actuation experiment displayed in the images can be seen in Figure 3C, where the red circles highlight the displacement at the time specifications of Figure 3B. Furthermore, the simulated displacement is also shown within the same plot, again showing good agreement with the experiment especially during the rise time of the coil current. At the peak current at 2.5 s, the actuator displacement also reaches a peak at 74.6 µm and afterward starts to decline as the coil current decreases. From this point on, there is a noticeable difference between the simulated and the measured displacement. In the experiment, the structure shows a much slower retraction and a constant displacement even after the coil current is 0 mA. This is however not caused by plastic deformations of the spring but by the hysteretic behavior of the FeNi-tube. The resulting magnetic field affecting the microactuator is therefore slightly increased during the fall time in comparison to the rise time. Lastly, residual magnetization of the tube results in a residual force and thus a constant displacement after the actuation. For the simulation, magnetic hysteresis was not considered as a tradeoff between model accuracy and calculation time, which is why the effects are not observable. However, there is still a slight offset at the end of the triangle pulse due to the viscoelastic relaxation of the spring. This means that viscoelasticity on one hand and magnetic hysteresis on the other are ultimately causing a hysteretic behavior of the microactuator. Additionally, the viscoelastic effects and the aforementioned displacement dependence of the magnetic force are affecting each other and result in a non-linear behavior of the actuator displacement.

The hysteresis of the actuator can also be seen in Figure 3D. We measured the microactuator displacement during the

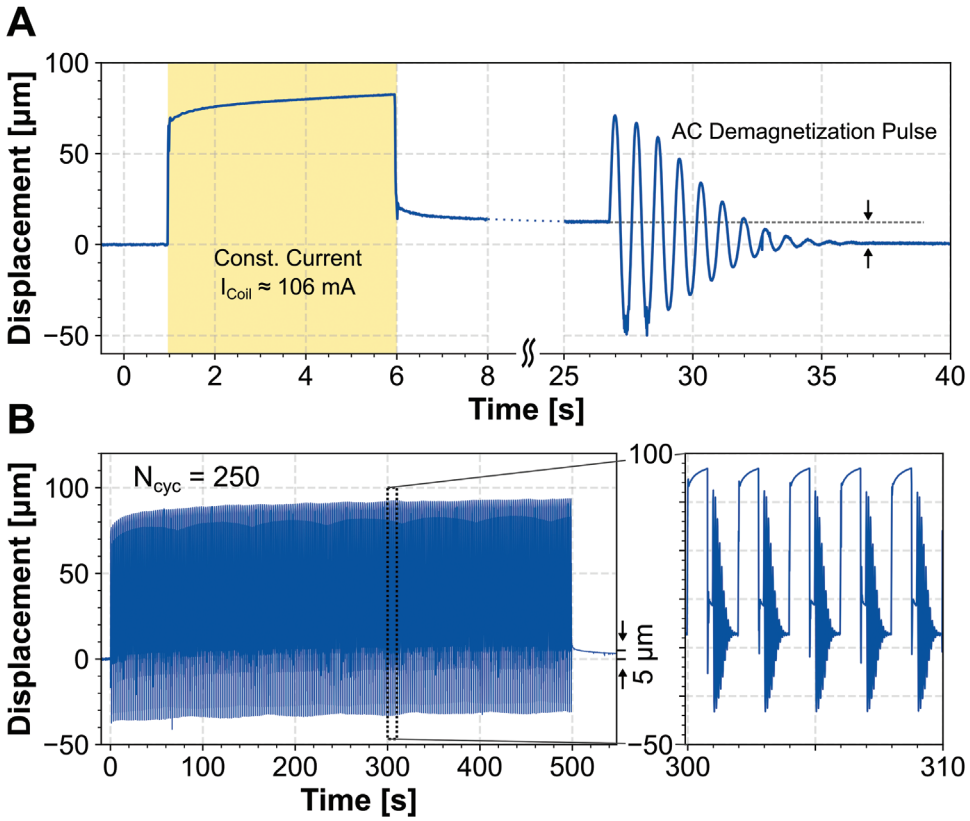

Figure 4. Experimental studies of demagnetization and repeatability. A) Displacement measurement where a constant coil current of 106 mA was applied for five seconds, resulting in a constantly displaced actuator due to the tube core magnetization. Shortly after, an alternating current (AC) demagnetization pulse with 10 s duration was applied. This pulse consists of a sine-wave with a Gaussian envelope, which is also observable in the displacement measurement since the microactuator follows the varying magnetic field. Afterward, the microactuator is reset to its original position. B) Repeatability measurement of 250 cycles, where one cycle consists of a 1 s rectangular pulse followed by a 1 s AC demagnetization pulse. Five of those pulses are shown in the zoomed-in region on the right side. A residual displacement smaller than 5 µm +can be seen 60 s after the last cycle.

actuation with symmetric triangle-pulses with a duration of 1, 5, 10, and 100 s. Numerical finite element simulations with 5 and 100 s are also included. It can be seen that the simulations slightly underestimates the peak displacement in case of a short actuation duration and slightly overestimates it in case of a longer actuation duration. This model inaccuracy might be attributed to a differing spring wire cross-section or deviations of the material viscoelasticity parameters. The lower sites of the curves correspond to a rising current and vice versa the upper sites to a falling current, as it is depicted by the arrows. It can be seen that there is a non-linear dependence between the displacement and the coil current that does also depend on the duration of the pulse. As a consequence, the measured displacement at the peak current ranges from 69.5 µm with a pulse-duration of 1 s to 88.9 µm with a pulse-duration of 100 s. This is due to the viscoelastic creep that causes an increased displacement over time, leading to a larger magnetic force and again to further displacement. Since these two effects can amplify each other, it is possible that larger coil currents or longer pulse durations result in collapse of the mechanical spring. Differences between displacements at rising and falling currents are increasing with pulse duration, meaning that viscoelasticity is also influencing the hysteresis. This is especially clear when comparing the two simulated curves because they are not affected by the magnetic hysteresis. Eventually, this does also lead to differences in the remaining offset, which of course is more severe in the experiment due to the residual magnetization of the tube.

In order to clear the residual magnetization, we tested if an alternating current (AC) demagnetization pulse could be applied after actuation. **Figure** 4A shows the microactuator displacement of this experiment. Here, we used a rectangular current pulse with a constant coil current of 106 mA held for 5 s. Again, viscoelastic creep and relaxation can be observed during and after the pulse. Interestingly, the microactuator also overshoots when the current is switched on and off, followed by short regions of damped oscillations. As expected, the actuator is constantly displaced after the pulse, remaining at around 12.5 µm. Following this, we applied an AC pulse to the coil consisting of a sine wave with Gaussian envelope of 10 s duration. Since the microactuator follows this current variation, it is also observable in the displacement measurement. It can be seen that the displacement reaches 0µm after demagnetization and the microactuator successfully returned to its initial position. It is worth mentioning that a small residual magnetization of the tube might remain. Its magnitude should however stay roughly the same every time the pulse is applied, regardless of the current profiles applied before. Thus, this method can be used to set an initial state of the actuator.

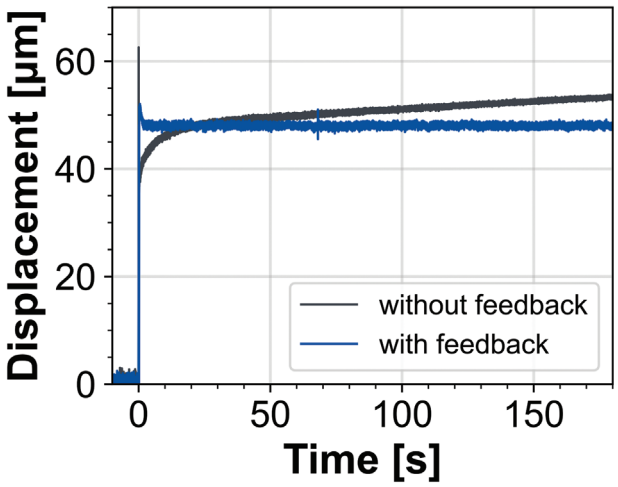

Figure 5. Displacement measurement of the microactuator during a step actuation with and without implemented closed-loop control.

To further study the microactuator, we conducted a repeatability measurement, shown in Figure 4B. We applied 250 cycles of a 1 s rectangular current pulse at 106 mA followed by a 1 s demagnetization pulse. The zoomed-in view on the right side shows 5 of those cycles and as it can be seen, the short demagnetization pulse duration is sufficient to strongly reduce the effect of tube magnetization. However, by looking at the entire repeatability measurement, it is obvious that viscoelasticity of the spring causes a change in displacement of succeeding cycles. As a result, there is a difference of approximately 16.7 µm regarding the peak displacement of the first and last cycle, while a difference of 10µm is already noticed after the first 30 cycles. This is caused by the short duration of the cycles, which is shorter than the relaxation time of the spring. It can be observed that the spring is recovering after the 250 cycles, such that the actuator offset is already below 5µm after a waiting time of 60 s. Despite not being a long-term or high repetition test, it can be observed that the actuator did not fully retract to its original position. It is therefore possible that the spring has already undergone plastic deformation.

Since the viscoelastic behavior poses a limiting factor regarding accurate, fast and repeatable positioning, we implemented a closed-loop feedback using a PI-controller. This is also a well-established method for dielectric elastomer actuators (DEA) that suffer from viscoelasticity as well.[60–63] A displacement measurement is plotted in **Figure 5** for the two cases of a step with and without feedback control. The target was set to 48 µm, which was reached by the actuator after 2 s and constantly held during the entire measurement duration. Hence, the viscoelastic behavior of the microactuator is successfully compensated by the controller. For the actuation without feedback, we used a step to an approximate coil current that yields a comparable displacement (see Experimental Section). A direct comparison is therefore not valid, but it can be seen that a constant displacement was not reached due to creep. Furthermore, overshooting and oscillations can again be observed within a time frame of 100 ms after the step occurred. As the sample rate of the distance sensor is not sufficient to resolve these oscillations, they can not be compensated by the controller. This means however that there is only a technical limitation and reachable response times of the actuator can be even shorter than what has been demonstrated.

3. Conclusion and Outlook

In conclusion, we presented the fabrication of a novel axially displacing magnetic microactuator and thoroughly studied its characteristics. For the first time, viscoelastic properties of the microactuator were extracted by nanoindentation tests of bulk IP-S and numerical simulation of the 3D-structure. Both, material and spring characteristics show good agreement with the generalized Kelvin-Voigt model. Since our material studies focused on structures fabricated with one specific parameter set, it could be interesting for future work how the viscoelastic behavior changes depending on the DC. This could then be used to further tweak the microactuator design.

The viscoelastic properties obtained through the mechanical characterization have been used in finite element simulations to accompany actuation experiments, which helps to understand the underlying processes. The numerical simulations showed good agreement with the measured data. We showed that the actuation is influenced by viscoelasticity on one hand and by magnetic hysteresis of the core material on the other. This results in a hysteresis and non-linearity of the microactuator displacement in dependence of the coil current as well as the actuation duration. We demonstrated that these limitations can be overcome by application of AC demagnetization pulses between actuations as well as implementation of a closed-loop control. In this way, precise positioning and position holding was achieved. Moreover, a response time of 2 s was demonstrated, limited only by technical aspects. Further improvement could therefore be the implementation of an open-loop control, for example as it has been already demonstrated for DEAs.[62,63]

In comparison to other additive manufactured microactuators, the herein presented one combines compactness and large deformations. With a diameter of 500 µm, it is in a size range not attainable with FDM even when accounting for the external microcoil. The range of motion can exceed 100 µm if higher coil currents are applied. As it could be seen, however, small deviations of the rectangular spring wire cross section lead to a significantly higher spring stiffness. Future design studies should therefore investigate these shape deviations e.g., though electron-microscopy measurements, allowing for a more accurate prediction of the microactuator displacement. In addition, the numerously observed tilting of the fabricated actuators due to inhomogeneous particle distributions inside the reservoir might be circumvented by separation of the reservoir into three chambers. By filling these chambers separately, we expect a balanced distribution and thus magnetic force exerted on the magnet.

The demonstrated microactuator was designed for axial motion and allows for large displacement with precise positioning. It is thus particularly interesting for, but not limited to applications in the field of 3D-printed microoptics, e.g., scanning, autofocus, or zoom. The fabrication method offers great flexibility toward the actuator design, enabling implementation of more sophisticated mechanical designs that can even be fabricated and actuated on optical fiber-tips for endoscopic applications. Following this, we believe that this actuation method facilitates novel designs in the field of 3D-printed microgrippers and -robotics.

4. Experimental Section

2PP Fabrication: The microactuators as well as the blocks for the nanoindentation tests were 3D-printed using the Photonic Professional GT2 (Nanoscribe GmbH & Co. KG). The proprietary resin IP-S was used for all structures. The 3D-models were sliced and hatched prior to printing with a slicing-distance of 0.2 µm and a hatching distance of 0.5 µm. They were fabricated with a 25X microscope objective with a numerical aperture of 0.8 and a long working distance of approximately 0.8 mm. For the writing process, a laser power of 50 % (corresponding to 25 mW) and a galvo-scanning speed of 100000 µm s^{-1} was mainly used. Several blocks for the nanoindentation test were also printed with a laser power of 60 % (corresponding to 30 mW). Polymerized structures were developed in PGMEA (AZ EBR Solvent, Microchemicals GmbH) for 12 min and afterward rinsed with isopropyl alcohol for 2 min and carefully dried with an air-blower.

The microactuators were printed onto a microscope cover glass with a measured thickness of approximately 155 µm. The blocks for nanoindenter measurements were printed onto a polished silicon substrate.

Microactuator Post-Processing: For the removal of sacrificial support structures and filling of the magnetic composite, a micromanipulator setup consisting of a motorized X-Y-Z-stage and two cameras for observation in x- and y-direction was used. The magnetic composite consists of NdFeB-microparticles (MQFP-14-12, Magnequench GmbH) with a typical grain size of 5 µm and a two-component epoxy resin (Epox 200G + Haerter 120L, DD Composite GmbH) with a viscosity lower than 780 mPa s. The particles and the epoxy resin are mixed in a weight ratio of 5:2 using a vibrating test tube shaker for 60 s. A piece of fiber was then used to gather droplets of the composite and fill the reservoir. The composite was then cured for at least 24 h. Afterward, the composite was magnetized within a uni-form magnetic field of approximately 4 T using a custom magnetization coil and an industrial pulse-magnetizer (MC2K10, MAGSYS magnet systeme GmbH).

SQUID Measurements: Six static structures were 3D-printed onto a single substrate. These structures had the same reservoir volume as the microactuator and the reservoirs were filled with composite of equal mixing ratio. A MPMS3 (Quantum Design GmbH) SQUID magnetometer was used to acquire the hysteresis curve of the samples. As the measurement yields the magnetic moment m_{mag} of all samples, the corresponding magnetic polarization J_{mag} for a single reservoir was evaluated by:

$$J_{mag} = \frac{m_{mag}}{N_{sample} \times V_{sample} \times c} \times 4\pi \times 10^{-4}\mathrm{T} \tag{2}$$

where N_{sample} is the number of samples, V_{sample} is the volume of the reservoir and c is a correction factor for the volume that accounts for overfilling and was estimated to be 1.20. four samples broke during the process, leaving only two for the measurement. However, other samples with slightly different reservoir volumes were also measured that showed nearly the same results (see Figure S5, Supporting Information).

In addition, the initial curve and magnetic hysteresis of the FeNi-tube core were measured, which is shown in Figure S6, (Supporting Information). A slight shift of the curves by approximately 70 Oe was noticed, which might be due to demagnetization fields occuring during the measurement. For the use of the measured initial curve in simulations, this offset was subtracted.

Nanoindentation Tests: A G200 (KLA Corp.) equipped with a conospherical diamond tip (Synton MDP, Switzerland) with a radius of 25 µm was used for the nanoindentation studies of the bulk IP-S blocks. Prior to each measurement, calibration of thermal drift and compliance were performed. In total, 7 blocks were measured using a load rate of 500 mN s^{-1} until a target displacement of 500 nm was reached. Following this, the load was held constant for 100 s and gradually reduced afterward.

Finite Element Simulations: Finite element simulations were conducted in COMSOL Multiphysics, including the Structural Mechanics and AC/DC modules. Mechanical simulations of the microactuator were conducted assuming a linear viscoelastic material behavior defined by the GKV model with the viscoelastic material parameters E_i and τ_i obtained though fitting of the nanoindenter measurements. From this simulation, the spring characteristics were obtained by applying a ramp and hold load profile (Equation (1)) with a target load of 25 µN, a ramp duration of 10 s and a hold duration of 50 s to the center surface boundary at the top. The arbitrarily selected target load of 25 µN was derived from prior static magnetic simulations, which provided an estimate of the expected magnetic force magnitude. The spring feet were defined as fixed boundary. A free triangular mesh with a maximum element size of 13 µm for the entire geometry was chosen and found to be sufficient.

For the simulation of actuation experiment, a rotationally symmetric 2D geometry model representing the experimental setup was implemented. This included the permanent magnet inside the reservoir, the microcoil with FeNi tube core, as well as a surrounding air domain. Magnetic field generated by the coil, as well as the permanent magnet were calculated through Ampres law. The magnetized composite inside the reservoir was assumed to be a permanent magnet with a remanence of 215 mT according to the hysteresis measurement. Regarding the FeNi-tube core of the microcoil, the magnetic behavior follows the *B-H*-relation of the measured initial magnetization curve. The magnetic body forces exerted on the permanent magnet was calculated through the Maxwell stress tensor. This leads to its displacement defined by a moving mesh environment, which obeys a set of relationships given by the two-element GKV-model:

$$\begin{aligned} h &= h_0 + h_1 + h_2 \\ F &= F_0 = F_1 = F_2 \\ F_0 &= k_0 h_0 \\ F_1 &= k_1\left(h_1 + \tau_1 \frac{dh_1}{dt}\right) \\ F_2 &= k_2\left(h_2 + \tau_2 \frac{dh_2}{dt}\right) \end{aligned} \tag{3}$$

where h is the total displacement and F the magnetic force with the subscripts denoting respective elements. The spring constants k_i and relaxation times τ_i correspond to the evaluated values shown in Figure 2D. The mesh was refined, resulting in a very fine mesh inside the permanent magnet, as well as in the gap between coil and the magnet with a maximum element size of 1 µm. It was to note that the influence of mass had been neglected in order to simplify the simulation.

Actuation Experiments: Actuation experiments were conducted using the same micromanipulation setup as for the microactuator post-processing. The chromatic confocal distance sensor (CHRocodile S, Precitec GmbH) with a measurement range of 300 µm was attached to the Z-axis of the stage. An additonal setup consisting of a mechanical precision X-Y-stage holding the microcoil and a fixture for the substrate with the microactuators was placed on the motorized X-Y-stage of the micromanipulator setup. This was necessary to enable the separation of the alignment between the microcoil and the microactuator, as well as the alignment between the microactuator and the distance sensor. To precisely align the microcoil with the actuator, a digital microscope (VHX7000, Keyence Corp.) was used. After alignment of the microactuator and the distance sensor, this study were able to simultaneously measure the displacement and observe with a digital camera. An illustration of the setup is shown in Figure S4 (Supporting Informations). As most microactuator samples suffered from significant tilt during actuation and thus could falsify measurements, the actuator showing the least amount of tilt was chosen for characterization.

For the actuation, current profiles were applied to the microcoil using an arbitrary waveform generator (DG1022, RIGOL Technologies, Inc.). The coil current was measured with a digital multimeter and limited to ±106 mA with an external potentiometer to avoid damaging of both microcoil and microacutator. The current behavior was measured with a constant current at the upper limit for 400 s and noticed drops up to -2.7 mA probably caused by joule heating. As this effect was less significant for triangular current profiles, a linear current over time relationship was assumed. The

two-layered microcoil had a length of 5 mm and consists of 170 windings in total. It was fabricated from isolated copper wire with a diameter of 50 µm, which was directly wound around the FeNi-tube core, using a custom winding setup. The tube core had a length of 20 mm, an outer diameter of 610 µm and a wall thickness of 50 µm. According to an EDX analysis, the alloy of the tube was comprised of 45% nickel and 55% iron.

Closed-Loop Control: A current source was designed containing a programmable microcontroller board (Arduino Nano, Arduino) to implement a closed-loop feedback for the actuation. The controller takes a ten-bit input value corresponding to the target displacement, which was compared to the measured displacement given by the distance sensor. Then, the output coil current was internally calculated using an open source PID-controller (AutoPID) library. It was found that a PI-controller was sufficient for this application, since the differential component did not significantly improve the response. The proportional parameter K_P and the integral parameter K_I were empirically evaluated to achieve a fast response and reduced overshooting. To avoid strong jumps of the actuator, the integral part was chosen larger than the proportional part, which ultimately led to $K_P = 0.2$ and $K_I = 16$. The response time was ultimately constrained by the scanning rate of the sensor rather than the speed of the Arduino board. For comparison between the controlled and uncontrolled step, the 12-bit value was read out corresponding to the output current during controlled actuation until a more stable state was reached. This value was then used for the step shown in Figure 5.

Supporting Information

Supporting Information is available from the Wiley Online Library or from the author.

Acknowledgements

The authors acknowledged funding of our research by the Deutsche Forschungsgemeinschaft (DFG, German Research Foundation) - Project 461765984. The authors furthermore like to thank Christian Grüner and Lukas Elbracht from the Institute of Electrical Energy Conversion, University of Stuttgart for providing their equipment and assisting with the magnetization of the microactuator samples.

Open access funding enabled and organized by Projekt DEAL.

Conflict of Interest

The authors declare no conflict of interest.

Data Availability Statement

The data that support the findings of this study are available from the corresponding author upon reasonable request.

Keywords

3D-printing, magnetic microactuator, nanoindentation, two-photon polymerization, viscoelasticity

Received: December 20, 2023
Revised: March 12, 2024
Published online:

[1] A. S. Algamili, M. H. M. Khir, J. O. Dennis, A. Y. Ahmed, S. S. Alabsi, S. S. Ba Hashwan, M. M. Junaid, *Nanoscale Res. Lett.* **2021**, *16*, 16.
[2] F. A. Mohd Ghazali, M. N. Hasan, T. Rehman, M. Nafea, M. S. Mohamed Ali, K. Takahata, *J. Micromechanics Microengineering* **2020**, *30*, 073001.
[3] A. P. Taylor, J. Izquierdo Reyes, L. F. Velásquez-García, *J. Phys. D. Appl. Phys.* **2020**, *53*, 355002.
[4] H. Hassanin, G. Sheikholeslami, P. Sareh, R. B. Ishaq, *Adv. Eng. Mater.* **2021**, *23*, 2100422.
[5] O. Ulkir, I. Ertugrul, N. Akkus, S. Ozer, *J. Mater. Eng. Perform.* **2022**, *31*, 8148.
[6] M. Dehghan, M. Tahmasebipour, S. Ebrahimi, *Microelectron. Eng.* **2022**, *254*, 111695.
[7] L. Li, A. Tirado, I. C. Nlebedim, O. Rios, B. Post, V. Kunc, R. R. Lowden, E. Lara-Curzio, R. Fredette, J. Ormerod, T. A. Lograsso, M. P. Paranthaman, *Sci. Rep.* **2016**, *6*, 36212.
[8] C. Huber, C. Abert, F. Bruckner, M. Groenefeld, S. Schuschnigg, I. Teliban, C. Vogler, G. Wautischer, R. Windl, D. Suess, *Sci. Rep.* **2017**, *7*, 9419.
[9] A. P. Taylor, C. Velez Cuervo, D. P. Arnold, L. F. Velasquez-Garcia, *J. Microelectromechanical Syst.* **2019**, *28*, 481.
[10] R. Bayaniahangar, S. Bayani Ahangar, Z. Zhang, B. P. Lee, J. M. Pearce, *Sens. Actuators B Chem.* **2021**, *326*, 128781.
[11] I. Bernardeschi, M. Ilyas, L. Beccai, *Adv. Intell. Syst.* **2021**, *3*, 2100051.
[12] Z. Lao, N. Xia, S. Wang, T. Xu, X. Wu, L. Zhang, *Micromachines* **2021**, *12*, 465.
[13] H. Jia, J. Flommersfeld, M. Heymann, S. K. Vogel, H. G. Franquelim, D. B. Brückner, H. Eto, C. P. Broedersz, P. Schwille, *Nat. Mater.* **2022**, *21*, 703.
[14] F. Rajabasadi, S. Moreno, K. Fichna, A. Aziz, D. Appelhans, O. G. Schmidt, M. Medina–Sánchez, *Adv. Mater.* **2022**, *34*, 2204257.
[15] M. F. Jamil, M. Pokharel, K. Park, *Appl. Sci.* **2022**, *12*, 11013.
[16] M. Power, A. J. Thompson, S. Anastasova, G.-Z. Yang, *Small* **2018**, *14*, 1703964.
[17] M. Power, A. Barbot, F. Seichepine, G.-Z. Yang, *Adv. Intell. Syst.* **2023**, *5*, 2200121.
[18] J. Li, M. Pumera, *Chem. Soc. Rev.* **2021**, *50*, 2794.
[19] S. R. Dabbagh, M. R. Sarabi, M. T. Birtek, S. Seyfi, M. Sitti, S. Tasoglu, *Nat. Commun.* **2022**, *13*, 5875.
[20] M. Kaynak, P. Dirix, M. S. Sakar, *Adv. Sci.* **2020**, *7*, 2001120.
[21] C. Liao, C. Xiong, J. Zhao, M. Zou, Y. Zhao, B. Li, P. Ji, Z. Cai, Z. Gan, Y. Wang, Y. Wang, *Light Adv. Manuf.* **2022**, *3*, 5.
[22] M. Zou, C. Liao, S. Liu, C. Xiong, C. Zhao, J. Zhao, Z. Gan, Y. Chen, K. Yang, D. Liu, Y. Wang, Y. Wang, *Light Sci. Appl.* **2021**, *10*, 171.
[23] S. Pagliano, D. E. Marschner, D. Maillard, N. Ehrmann, G. Stemme, S. Braun, L. G. Villanueva, F. Niklaus, *Microsyst. Nanoeng.* **2022**, *8*, 105.
[24] J. C. Williams, H. Chandrahalim, J. S. Suelzer, N. G. Usechak, *Adv. Photonics Res.* **2022**, *3*, 2100359.
[25] H. Lee, F. Seichepine, G. Yang, *Adv. Funct. Mater.* **2020**, *30*, 2002510.
[26] A. Münchinger, V. Hahn, D. Beutel, S. Woska, J. Monti, C. Rockstuhl, E. Blasco, M. Wegener, *Adv. Mater. Technol.* **2022**, *7*, 2100944.
[27] M. del Pozo, C. Delaney, M. Pilz da Cunha, M. G. Debije, L. Florea, A. P. H. J. Schenning, *Small Struct.* **2022**, *3*, 2100158.
[28] T. Spratte, S. Geiger, F. Colombo, A. Mishra, M. Taale, L. Hsu, E. Blasco, C. Selhuber–Unkel, *Adv. Mater. Technol.* **2023**, *8*, 2200714.
[29] C. Zheng, F. Jin, Y. Zhao, M. Zheng, J. Liu, X. Dong, Z. Xiong, Y. Xia, X. Duan, *Sens. Actuators, B* **2020**, *304*, 127345.
[30] B. Ahmad, A. Barbot, G. Ulliac, A. Bolopion, *IEEE/ASME Trans. Mechatron.* **2022**, *27*, 4090.
[31] A. Münchinger, L.-Y. Hsu, F. Fürniß, E. Blasco, M. Wegener, *Mater. Today* **2022**, *59*, 9.
[32] L. Hsu, P. Mainik, A. Münchinger, S. Lindenthal, T. Spratte, A. Welle, J. Zaumseil, C. Selhuber–Unkel, M. Wegener, E. Blasco, *Adv. Mater. Technol.* **2023**, *8*, 2200801.
[33] J. Wang, F. Jin, X. Dong, J. Liu, M. Zheng, *Adv. Mater. Technol.* **2022**, *7*, 2200276.

[34] L. Zhang, B. Liu, C. Wang, C. Xin, R. Li, D. Wang, L. Xu, S. Fan, J. Zhang, C. Zhang, Y. Hu, J. Li, D. Wu, L. Zhang, J. Chu, *Nano Lett.* **2022**, *22*, 5277.
[35] M. del Pozo, C. Delaney, C. W. M. Bastiaansen, D. Diamond, A. P. H. J. Schenning, L. Florea, *ACS Nano* **2020**, *14*, 9832.
[36] J. Wang, F. Jin, X. Dong, J. Liu, M. Zhou, T. Li, M. Zheng, *Small* **2023**, *19*, 2303166.
[37] R. K. Jayne, T. J. Stark, J. B. Reeves, D. J. Bishop, A. E. White, *Adv. Mater. Technol.* **2018**, *3*, 1700293.
[38] S. Kim, C. Velez, R. S. Pierre, G. L. Smith, S. Bergbreiter, *J. Microelectromech. Syst.* **2020**, *29*, 544.
[39] S. Kim, R. Kubicek, S. Bergbreiter, *Adv. Funct. Mater.* **2023**, 2304991.
[40] S. Kim, S. Lee, J. Lee, B. J. Nelson, L. Zhang, H. Choi, *Sci. Rep.* **2016**, *6*, 30713.
[41] P. Liao, L. Xing, S. Zhang, D. Sun, *Small* **2019**, *15*, 1901197.
[42] V. Vieille, R. Pétrot, O. Stéphan, G. Delattre, F. Marchi, M. Verdier, O. Cugat, T. Devillers, *Adv. Mater. Technol.* **2020**, *5*, 2000535.
[43] F. Rothermel, S. Thiele, C. Jung, H. Giessen, A. Herkommer, *Proc. SPIE* **2021**, *11816*, 118160I.
[44] X. Hu, I. C. Yasa, Z. Ren, S. R. Goudu, H. Ceylan, W. Hu, M. Sitti, *Sci. Adv.* **2021**, *7*, eabe8436.
[45] N. Geid, J. U. Leutner, O. Prucker, J. Rühe, *Actuators* **2023**, *12*, 124.
[46] S. Zhang, X. Hu, M. Li, U. Bozuyuk, R. Zhang, E. Suadiye, J. Han, F. Wang, P. Onck, M. Sitti, *Sci. Adv.* **2023**, *9*, eadf9462.
[47] R. Pétrot, T. Devillers, O. Stéphan, O. Cugat, C. Tomba, *Adv. Funct. Mater.* **2023**, *33*, 49.
[48] J. S. Oakdale, J. Ye, W. L. Smith, J. Biener, *Opt. Express* **2016**, *24*, 27077.
[49] J. Bauer, A. Guell Izard, Y. Zhang, T. Baldacchini, L. Valdevit, *Adv. Mater. Technol.* **2019**, *4*, 1900146.
[50] I. S. Ladner, M. A. Cullinan, S. K. Saha, *RSC Adv.* **2019**, *9*, 28808.
[51] M. Diamantopoulou, N. Karathanasopoulos, D. Mohr, *Addit. Manuf.* **2021**, *47*, 102266.
[52] S. Schweiger, T. Schulze, S. Schlipf, P. Reinig, H. Schenk, *J. Opt. Microsyst.* **2022**, *2*, 033501.
[53] K. Tao, J. Wu, A. G. P. Kottapalli, D. Chen, Z. Yang, G. Ding, S. W. Lye, J. Miao, *Solid. State. Electron.* **2017**, *138*, 66.
[54] S. Sarkar, P. J. Baker, E. P. Chan, S. Lin-Gibson, M. Y. M. Chiang, *Soft Matter* **2017**, *13*, 3975.
[55] J. Kubacková, C. Slabý, D. Horvath, A. Hovan, G. T. Iványi, G. Vizsnyiczai, L. Kelemen, G. Žoldák, Z. Tomori, G. Bánó, *Nanomaterials* **2021**, *11*, 2961.
[56] J. Rosenbohm, G. Minnick, B. T. Safa, A. M. Esfahani, X. Jin, H. Zhai, N. V. Lavrik, R. Yang, *Biomed. Microdevices* **2022**, *24*, 33.
[57] A. Groetsch, S. Stelzl, Y. Nagel, T. Kochetkova, N. C. Scherrer, A. Ovsianikov, J. Michler, L. Pethö, G. Siqueira, G. Nyström, J. Schwiedrzik, *Small* **2023**, *19*, 2202470.
[58] H. Lu, B. Wang, J. Ma, G. Huang, H. Viswanathan, *Mech. Time-Depend. Mater.* **2003**, *7*, 189.
[59] T. Gissibl, S. Thiele, A. Herkommer, H. Giessen, *Nat. Photonics* **2016**, *10*, 554.
[60] G. Rizzello, D. Naso, A. York, S. Seelecke, *Smart Mater. Struct.* **2016**, *25*, 035034.
[61] R. Zhang, P. Iravani, P. Keogh, *Sens. Actuators, A* **2017**, *264*, 123.
[62] J. Zou, G.-Y. Gu, L.-M. Zhu, *IEEE/ASME Trans. Mechatron.* **2017**, *22*, 51.
[63] A. Poulin, S. Rosset, *Extrem. Mech. Lett.* **2019**, *27*, 20.